

Hydrogen-bearing iron peroxide and the origin of ultralow-velocity zones

Jin Liu^{1*}, Qingyang Hu^{1,2*}, Duck Young Kim², Zhongqing Wu³, Wenzhong Wang³, Yuming Xiao⁴, Paul Chow⁴, Yue Meng⁴, Vitali B. Prakapenka⁵, Ho-Kwang Mao^{2,6} & Wendy L. Mao^{1,7}

Ultralow-velocity zones (ULVZs) at Earth's core–mantle boundary region have important implications for the chemical composition and thermal structure of our planet, but their origin has long been debated^{1–3}. Hydrogen-bearing iron peroxide (FeO₂H_x) in the pyrite-type crystal structure was recently found to be stable under the conditions of the lowermost mantle^{4–6}. Using high-pressure experiments and theoretical calculations, we find that iron peroxide with a varying amount of hydrogen has a high density and high Poisson ratio as well as extremely low sound velocities consistent with ULVZs. Here we also report a reaction between iron and water at 86 gigapascals and 2,200 kelvin that produces FeO₂H_x. This would provide a mechanism for generating the observed volume occupied by ULVZs through the reaction of about one-tenth the mass of Earth's ocean water in subducted hydrous minerals with the effectively unlimited reservoir of iron in Earth's core. Unlike other candidates for the composition of ULVZs^{7–12}, FeO₂H_x synthesized from the superoxidation of iron by water would not require an extra transportation mechanism to migrate to the core–mantle boundary. These dense FeO₂H_x-rich domains would be expected to form directly in the core–mantle boundary region and their properties would provide an explanation for the many enigmatic seismic features that are observed in ULVZs^{1,13,14}.

The core–mantle boundary (CMB) represents a region with the largest compositional and rheological contrast within Earth, and it has a key role in the thermal and chemical evolution of the planet³. Seismological studies have revealed a number of thin, dense domains, with variable thicknesses of 5–40 km, lying directly above the CMB, called ULVZs, where seismic wave speeds are depressed by about 10% for P-waves (V_P) and by about 10%–30% for S-waves (V_S)^{1,13,14}. Most ULVZs appear as distinct domains within and near the margins of large low shear velocity provinces (LLSVPs), but some have been mapped far from LLSVPs, suggesting lateral thermal and compositional chemical heterogeneities at the base of the mantle¹⁵. In particular, the density increase of about 10% in ULVZs is probably due to the enrichment of heavy elements such as iron. Iron-enrichment in ULVZs may have an impact on core heat flow and thus on the generation and variability of the geomagnetic field⁷. Moreover, the velocity anomalies might indicate that ULVZs are partially molten, reflecting temperature anomalies or compositional heterogeneity in the region, which in turn could be the source of deep-mantle plumes^{14,16}.

Many previous studies have attributed ULVZs to partial melting⁷, although the presence of silicate melts in the CMB region is still debated, largely owing to the uncertainty of the mantle thermal structure near the CMB¹⁷ and the instability of a basal magma ocean¹⁸. Alternatively, accumulated silicate sediments from the core⁸, subducted banded iron formations⁹, iron-enriched mantle phases like

postperovskite¹⁰ and ferropericlasite¹¹, and iron–carbon metallic melts forming in the lowermost mantle¹² have also been proposed as possible explanations for the origins of ULVZs. We note that there may be more than one type of ULVZ, given that P- and S-wave velocity reductions and density increases vary among different ULVZs, indicating that different mechanisms may individually or jointly produce ULVZs within Earth¹³.

Iron peroxide (FeO₂) with the space group $Pa\bar{3}$ was recently found to form under the high pressure–temperature conditions relevant to Earth's lower mantle beneath 1,800 km through the partial dehydrogenation of goethite (α -FeOOH) or the reaction of hematite (Fe₂O₃) with H₂O (ref. 4). Further experiments⁵ demonstrated that a varying amount of hydrogen can diffuse into the FeO₂ lattice to form FeO₂H_x (with x from 0 to 1). The formation of the pyrite-type phase of FeOOH has recently been confirmed⁶ under pressure–temperature conditions of Earth's lower mantle. That work⁶ suggested that goethite (α -FeOOH) would transform into the pyrite-type high-pressure phase without loss of any hydrogen at pressure–temperature conditions up to 2,400 K at 111 GPa and 1,500 K at 129 GPa. The FeO₂H_x-bearing domains will be very different from the nominally bridgmanite–ferropericlasite mantle and may enable us to interpret many of the seismic and geochemical anomalies in the CMB region⁴. However, many of the physical properties of FeO₂H_x and its potential abundance within Earth are not well constrained. Here we have combined high-pressure experiments and first-principles calculations to study the formation mechanisms and sound velocities of FeO₂H_x in order to evaluate whether it would be a more plausible candidate for ULVZs.

We conducted *in situ* high-pressure synchrotron experiments on FeO₂H_x up to CMB pressures using a laser-heated diamond anvil cell (DAC) coupled with X-ray diffraction (XRD) at beamlines 16ID-B and 13ID-D and nuclear resonant inelastic X-ray scattering (NRIXS) at 16ID-D of the Advanced Photon Source, Argonne National Laboratory. In one run, a piece of iron foil was suspended in excess water in a Re gasket and was compressed in a DAC to 86 GPa at room temperature. XRD patterns before laser heating showed diffraction peaks only from iron and water. After the sample was heated with infrared lasers to 2,200 K, the diffraction peaks of iron were replaced with a number of new peaks that can be indexed with the pyrite-type phase of FeO₂H_x and the face-centred cubic (f.c.c.) phase of FeH (Fig. 1), demonstrating that FeO₂H_x can form through iron superoxidation by water under the pressure–temperature conditions of the deep lower mantle.

In the other three runs, starting materials of ⁵⁷Fe-enriched hematite (Fe₂O₃) in either H₂O or O₂ media were compressed in a DAC to about 90 GPa and laser-heated to 1,800–2,200 K to synthesize iron peroxide. XRD patterns were collected and showed sharp diffraction peaks

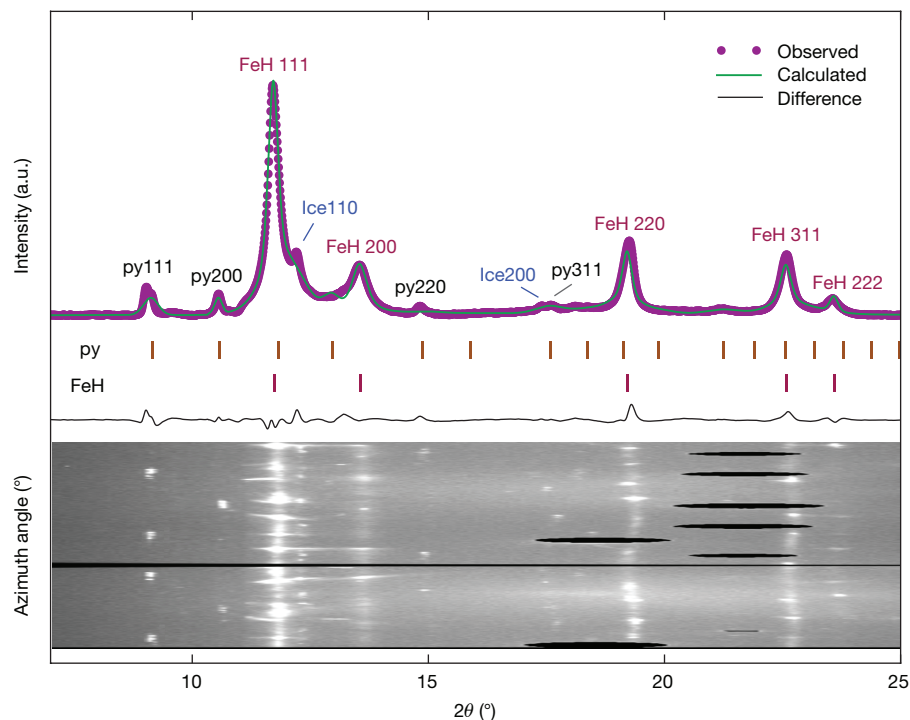
¹Department of Geological Sciences, Stanford University, Stanford, California 94305, USA. ²Center for High Pressure Science and Technology Advanced Research, Shanghai 201203, China.

³Laboratory of Seismology and Physics of Earth's Interior, School of Earth and Space Sciences, University of Science and Technology of China, Hefei, China. ⁴High Pressure Collaborative Access Team, Geophysical Laboratory, Carnegie Institution of Washington, Argonne, Illinois 60439, USA. ⁵Center for Advanced Radiation Sources, University of Chicago, Chicago, Illinois 60437, USA.

⁶Geophysical Laboratory, Carnegie Institution of Washington, Washington DC 20015, USA. ⁷Stanford Institute for Materials and Energy Sciences, SLAC National Accelerator Laboratory, Menlo Park, California 94025, USA.

*These authors contributed equally to this work.

Figure 1 | XRD pattern of reaction products of iron and water. Iron powder (Sigma-Aldrich CAS: 7439-89-6) was compressed in excess H₂O to 86 GPa at room temperature, then heated up to 2,200 K and finally quenched to 300 K. The XRD pattern was collected at 86 GPa and 300 K after laser heating with an X-ray wavelength of $\lambda = 0.4066 \text{ \AA}$. It was fitted by Rietveld refinement to the pyrite-type phase ($a = 4.4102(11) \text{ \AA}$), the quenchable high-temperature f.c.c. phase³⁰ of FeH ($a = 3.4445(3) \text{ \AA}$), and excess ice X. The R -factor is $wR_f = 0.146$; 'py' is the pyrite-type phase of FeO₂H_{*x*}; 'a.u.' is arbitrary units. Source Data for Figs 1–4 accompany the online version of the paper.



(Extended Data Fig. 1) in perfect agreement with the pyrite-type phase of iron peroxide. The diffraction peaks of iron peroxide (Extended Data Fig. 1) persisted up to the maximum pressure–temperature conditions of the present study (2,600 K at 133 GPa and 3,100–3,300 K at 125 GPa), showing that iron peroxide is stable under the pressure–temperature conditions relevant to the CMB. The XRD measurements were used for determinations of unit-cell volumes. For a given pressure, the unit cell of iron peroxide synthesized from Fe₂O₃ in pure O₂ is a constant, but that from Fe₂O₃ in H₂O is variable, indicating the variation of x in FeO₂H_{*x*} and $x = 0$ with the pure O₂ medium⁵. Theoretical calculations indicated that the volume of FeO₂H is approximately 9% larger than that of FeO₂ at room temperature (Fig. 2). Our FeO₂H_{*x*} lies between FeO₂ and FeO₂H from theoretical calculations (Fig. 2). According to ref. 5, the hydrogen concentration (x) was estimated to be 0.5–0.7 in the synthesized FeO₂H_{*x*} sample that was used for NRIXS experiments in the present study.

The partial phonon density of states (PDOS) was experimentally determined at 81 (± 2) GPa for FeO₂ and 133 (± 4) GPa for FeO₂H_{*x*} from NRIXS measurements at room temperature (Fig. 3). The peak positions for the PDOS from our high-pressure experiments are consistent with our theoretical calculations (inset to Fig. 3). The Debye sound velocity V_D of iron peroxide was extracted from its PDOS (Fig. 3). Then the V_P and V_S of FeO₂ and FeO₂H_{*x*} were determined from their V_D , density and isothermal bulk modulus (see Methods). The V_P of FeO₂H_{*x*} at 133 GPa and 300 K from NRIXS measurements is 11.32 (± 0.27) km s⁻¹, which is comparable to theoretical calculations, while the experimental V_S is 4.50 (± 0.07) km s⁻¹, which is relatively lower than the theoretical result (Extended Data Fig. 2). We note that there is an offset in the absolute values of the theoretical calculations from those of NRIXS experiments. Because conducting NRIXS experiments under conditions of simultaneous high pressure and high temperature is extremely challenging, the effects of temperature and hydrogen on the sound velocities of FeO₂H_{*x*} were extracted from theoretical calculations. In particular, our theoretical calculations showed that the V_S of FeO₂ is modified by <1% with the incorporation of hydrogen and slightly increases by approximately 5% from 5.29 km s⁻¹ at 60 GPa to 5.58 km s⁻¹ at 140 GPa at 300 K, while the incorporation of hydrogen may increase the V_P of FeO₂ by approximately 2%–3% between 60 GPa and 140 GPa at 300 K (Extended Data

Fig. 2). In particular, the effect of temperature on the sound velocities of FeO₂H is greater than for FeO₂ at 60–130 GPa (Extended Data Fig. 3). For example, our theoretical calculations suggest that the reductions of V_P and V_S are approximately 4% and 6% for FeO₂H and 3% and 4% for FeO₂, respectively, from 300 K to 3,000 K at 130 GPa (inset to Fig. 4).

The hydrogen content appears to have a weak influence on the sound velocities and Poisson ratio of FeO₂H_{*x*} at CMB conditions. Our theoretical calculations show that FeO₂H is approximately 1% faster in V_P and 3% slower in V_S in comparison to hydrogen-free FeO₂ at 3,000 K and 130 GPa (inset to Fig. 4). Assuming that the temperature dependence of the sound velocities of FeO₂ and FeO₂H determined from our theoretical calculations is applicable for our NRIXS experimental results at room temperature, the V_P and V_S of FeO₂H_{*x*} (with x from 0 to 1) have been extrapolated to 3,000 K and

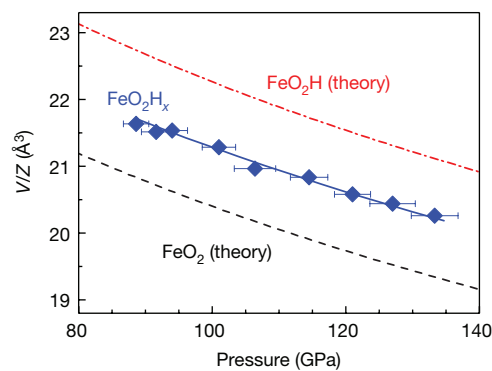


Figure 2 | Comparison of the pressure–volume relationships for FeO₂H_{*x*} at 300 K. The vertical axis is plotted as the unit cell volume per formula unit (V/Z). The number of molecules per unit cell (Z) is 4 for FeO₂H_{*x*}. Diamond symbols show the FeO₂H_{*x*} that was synthesized from Fe₂O₃ with H₂O (this study). The solid curve is the Birch–Murnaghan equation of state fitted to our experimental data for FeO₂H_{*x*}; dashed and dash-dotted curves are theoretical calculations for FeO₂ and FeO₂H, respectively (this study). The error bars for pressure are 95% confidence intervals. Error bars of the volume derived from XRD experiments are smaller than the symbol.

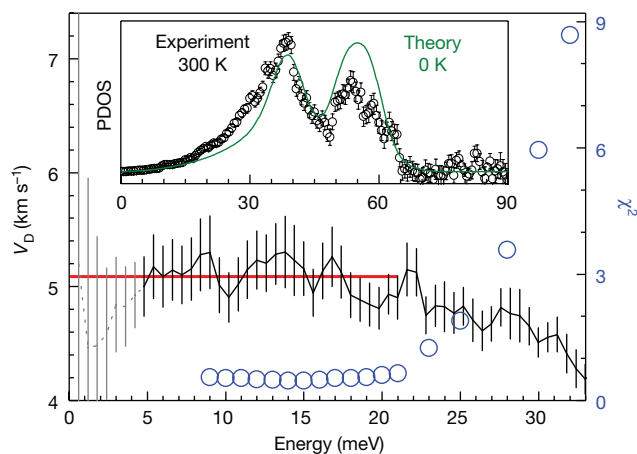


Figure 3 | NRIXS data for FeO_2H_x and determination of V_D at 133 GPa.

The solid and dashed curves reflect the low-energy region of the PDOS where the Debye-like behaviour is observed. The minimum energy of the fitted region (E_{\min}), illustrated by the onset of the solid curve, is larger than the measured resolution function. A χ^2 analysis of our parabolic fits was performed between E_{\min} and the maximum fitted energy, as shown by blue circles. The red line gives the best fit for the parabolic region between 4.8 meV and 21 meV. The inset shows the PDOS of FeO_2H_x (black circles) experimentally determined at 133 GPa compared with that of pyrite-type FeO_2H (green curve) theoretically calculated at 130 GPa. The error bars are 95% confidence intervals.

CMB pressures, yielding values of 10.90 km s^{-1} and 4.25 km s^{-1} , respectively (inset to Fig. 4). The extrapolated values have an uncertainty of 5%–10% when considering uncertainties from NRIXS measurements, the effect of temperature on sound velocities based on our theoretical calculations, and the hydrogen concentration of FeO_2H_x . In contrast, the incorporation of hydrogen can greatly affect the density of iron peroxide. Our theoretical calculations suggest that FeO_2 is approximately 9% denser than FeO_2H at 130 GPa (Extended Data Fig. 4).

The velocity reductions in V_p and V_s for FeO_2H_x are approximately 20% and 42%, respectively, relative to the radially averaged one-dimensional seismic model (PREM)¹⁹ in the CMB region. The Poisson ratio of FeO_2H_x is 0.41, which is higher by approximately 35% compared to PREM. A mixture of 40%–50% FeO_2H_x with the ambient mantle will cause a decrease of about 10% in the V_p at the CMB, while reducing the V_s by 10%–30% when the large uncertainty on the V_s of

FeO_2H_x is considered. The density of this mixture is about 10% higher than that of PREM at the CMB. The changes in these parameters of FeO_2H_x -bearing domains can explain many of the seismic features of ULVZs (Fig. 4). Geodynamic simulations²⁰ suggested that not all of the subducted oceanic crust would descend to the CMB because thin domains cannot provide enough negative buoyancy to overcome mantle viscous stresses. Therefore, FeO_2H_x forming from goethite in the subducted oceanic crust might not reach ULVZs.

In addition to primordial water in Earth's deep mantle²¹, recent studies have shown that water on the surface may be transported in descending subducted plates to the base of the mantle in the form of aluminous hydrous silicates (for example, phase H)²². The hydrous partial melt from dehydration of hydrous minerals at the CMB might react with the Fe_2O_3 component of mantle silicates and subducted banded iron formations⁹ to form FeO_2H_x . Most importantly, the total quantity of FeO_2H_x is controlled by the available water when FeO_2H_x forms through the reaction of the iron core with water across the CMB. The estimated amount of water subducted globally is about $10^{12} \text{ kg yr}^{-1}$ (ref. 23), of which $7 \times 10^{11} \text{ kg yr}^{-1}$ returns to the surface through volcanism, and $3 \times 10^{11} \text{ kg yr}^{-1}$ is subducted past the volcanic front and can be delivered to the deeper mantle²⁴. To build ULVZs that contain 40%–50% FeO_2H_x with thicknesses of about 5–20 km over about 12% of the surface of the CMB⁹ would require only a flat rate of about $4.5 \times 10^{10} \text{ kg yr}^{-1}$ water reaching the CMB over the past 4.6 Gyr. A total mass of water of about $1.383 \times 10^{20} \text{ kg}$, corresponding to approximately one-tenth of the mass of water in Earth's oceans, is sufficient to form ULVZs. Therefore, with the nearly unlimited reservoir of iron in the core and a relatively modest amount of water, the formation mechanism of iron superoxidation by water described here is able to generate a volume of FeO_2H_x -rich domains at the CMB that is sufficient to explain the formation of ULVZs. Furthermore, our experimental results show that FeO_2H_x is stable at least up to 3,100–3,300 K at 125 GPa, indicating that this pyrite-type phase is stable at the pressure–temperature conditions of the base of the mantle⁶. Thus, FeO_2H_x does not melt and would be preserved on the mantle side of the CMB where the denser outer core (about 10 g cm^{-3}) prevents it from sinking further⁶. In contrast, iron hydride associated with hydrogen-bearing iron peroxide FeO_2H_x from the iron–water reaction at the CMB probably dissolves into the outer core, because the melting temperature of iron hydride is lower by around 1,000 K than that of mantle silicates and oxides²⁵. Therefore, FeO_2H_x provides a more compelling explanation for the origin of ULVZs than do either partial melting or the presence of iron-enriched anhydrous phases.

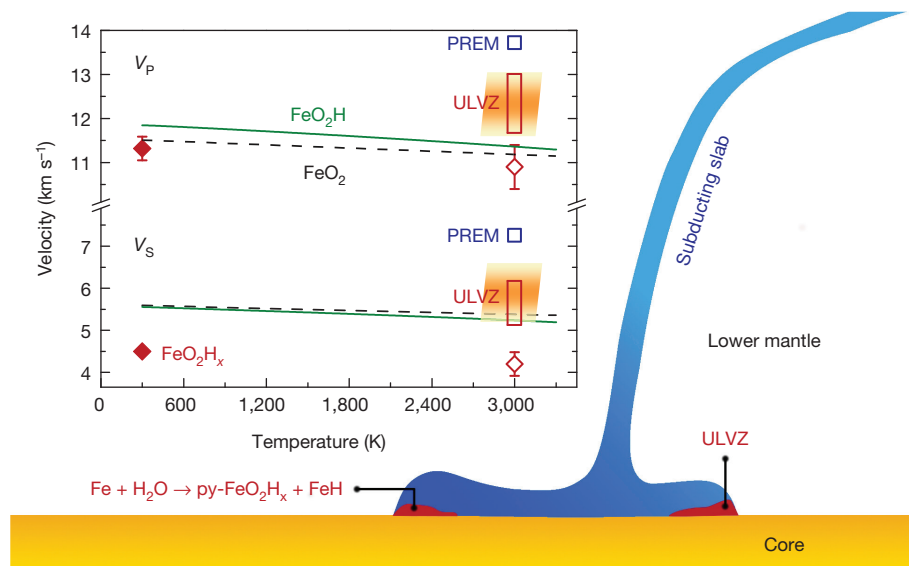


Figure 4 | Schematic diagram of the formation of FeO_2H_x -bearing domains at the CMB.

Water released from the slab (blue) reacts with the iron-rich outer core (orange) to form FeO_2H_x -bearing domains (red patches) at the CMB. The inset shows the sound velocities of FeO_2H_x at high pressure and high temperature. The solid and dashed curves are the theoretical calculations for FeO_2H and FeO_2 at 130 GPa. Filled diamonds show FeO_2H_x at 133 GPa from NRIXS experiments; open diamonds show FeO_2H_x extrapolated to 3,000 K and CMB pressures. Shaded areas show the extrapolated V_p and V_s of FeO_2H_x -bearing domains for a mixture of 40%–50% FeO_2H_x with the ambient mantle based on PREM (blue squares); the red rectangles indicate the reduction in V_p (5%–15%) and V_s (15%–30%) observed in ULVZs¹³. The error bars are 95% confidence intervals.

Recently, magnesium peroxide (MgO_2) has been found to be stable at the pressure–temperature conditions of the lowermost mantle²⁶. MgO_2 and FeO_2 may form a solid-solution series of $(\text{Fe,Mg})\text{O}_2$ at high pressures, in a way similar to other iron-rich oxides, for example, $(\text{Fe,Mg})\text{O}$ and $(\text{Fe,Mg})_3\text{Fe}_4\text{O}_9$ (ref. 27). In particular, Mg substitution for Fe in FeO_2H_x could reduce the density such that some ULVZs might be entirely composed of Mg-bearing FeO_2H_x . Furthermore, the pyrite-type phase of FeOOH was suggested to form a solid solution with AlOOH and MgSiO_4H_2 (phase H) at the lowermost mantle⁶. With its varying hydrogen concentration and potential incorporation of Mg, Al and Si, FeO_2H_x may have a substantial impact on mantle heterogeneity and dynamics. The potential incorporation of Mg, Al and Si into FeO_2H_x thus needs to be investigated, as well as their effects on the sound velocities and density of FeO_2H_x .

The presence of hydrogen in iron peroxide strongly affects its density and sound velocities; that is, the incorporation of hydrogen increases the V_p of iron peroxide but has an opposite effect on the V_s in the lowermost mantle. Such distinct effects of hydrogen on sound velocities may help to explain anti-correlated seismic velocity anomalies in the region¹⁵. Moreover, at the CMB, FeO_2H_x is in contact with the iron core where hydrogen may be abundant through alloying of hydrogen with iron in the early Earth²⁸. We can expect hydrogen migration across the CMB, with its direction depending on the partition coefficients of hydrogen between FeO_2H_x and Fe–H alloys, suggesting that the deep hydrogen cycle may involve the entire Earth. We could also expect FeO_2H_x to be enriched in heavy iron isotopes ($^{56}\text{Fe}/^{54}\text{Fe}$) owing to the presence of hydrogen and its superoxidation state, which may help to control the iron isotopic features of the deep Earth²⁹. The geochemical reservoirs in ULVZs may be entrained in mantle upwellings and transported to the surface¹⁴, where they would then contribute to the iron isotopic signature observed in terrestrial basalts.

Online Content Methods, along with any additional Extended Data display items and Source Data, are available in the online version of the paper; references unique to these sections appear only in the online paper.

Received 29 March; accepted 27 September 2017.

- Garnero, E. J. & Helmberger, D. V. Seismic detection of a thin laterally varying boundary layer at the base of the mantle beneath the central-Pacific. *Geophys. Res. Lett.* **23**, 977–980 (1996).
- Vidale, J. & Hedlin, M. Evidence for partial melt at the core–mantle boundary north of Tonga from the strong scattering of seismic waves. *Nature* **391**, 682–685 (1998).
- Hernlund, J. W. & McNamara, A. K. In *Treatise on Geophysics* 2nd edn, Vol. 7, 461–519 (Elsevier, 2015).
- Hu, Q. *et al.* FeO_2 and FeOH under deep lower-mantle conditions and Earth's oxygen–hydrogen cycles. *Nature* **534**, 241–244 (2016).
- Hu, Q. *et al.* Dehydrogenation of goethite in Earth's deep lower mantle. *Proc. Natl Acad. Sci. USA* **114**, 1498–1501 (2017).
- Nishi, M., Kuwayama, Y., Tsuchiya, J. & Tsuchiya, T. The pyrite-type high-pressure form of FeOOH . *Nature* **547**, 205–208 (2017).
- Williams, Q. & Garnero, E. J. Seismic evidence for partial melt at the base of Earth's mantle. *Science* **273**, 1528–1530 (1996).
- Buffett, B. A., Garnero, E. J. & Jeanloz, R. Sediments at the top of Earth's core. *Science* **290**, 1338–1342 (2000).
- Dobson, D. P. & Brodholt, J. P. Subducted banded iron formations as a source of ultralow-velocity zones at the core–mantle boundary. *Nature* **434**, 371–374 (2005).
- Mao, W. L. *et al.* Iron-rich post-perovskite and the origin of ultralow-velocity zones. *Science* **312**, 564–565 (2006).
- Wicks, J. K., Jackson, J. M. & Sturhahn, W. Very low sound velocities in iron-rich $(\text{Mg,Fe})\text{O}$: implications for the core–mantle boundary region. *Geophys. Res. Lett.* **37**, L15304 (2010).
- Liu, J., Li, J., Hrubicki, R. & Smith, J. S. Origins of ultra-low velocity zones through slab-derived metallic melt. *Proc. Natl Acad. Sci. USA* **113**, 5547–5551 (2016).
- Thorne, M. S. & Garnero, E. J. Inferences on ultralow-velocity zone structure from a global analysis of SPdKS waves. *J. Geophys. Res.* **109**, 2156–2202 (2004).
- McNamara, A. K., Garnero, E. J. & Rost, S. Tracking deep mantle reservoirs with ultra-low velocity zones. *Earth Planet. Sci. Lett.* **299**, 1–9 (2010).
- Garnero, E. J., McNamara, A. K. & Shim, S.-H. Continent-sized anomalous zones with low seismic velocity at the base of Earth's mantle. *Nat. Geosci.* **9**, 481–489 (2016).
- Thorne, M. S., Garnero, E. J., Jahnke, G., Igel, H. & McNamara, A. K. Mega ultra low velocity zone and mantle flow. *Earth Planet. Sci. Lett.* **364**, 59–67 (2013).
- Anzellini, S., Dewaele, A., Mezouar, M., Loubeyre, P. & Morard, G. Melting of iron at Earth's inner core boundary based on fast X-ray diffraction. *Science* **340**, 464–466 (2013).
- Thomas, C. W. & Asimow, P. D. Direct shock compression experiments on premolten forsterite and progress toward a consistent high-pressure equation of state for $\text{CaO-MgO-Al}_2\text{O}_3\text{-SiO}_2\text{-FeO}$ liquids. *J. Geophys. Res.* **118**, 5738–5752 (2013).
- Dziewonski, A. M. & Anderson, D. L. Preliminary reference Earth model. *Phys. Earth Planet. Inter.* **25**, 297–356 (1981).
- Li, M. & McNamara, A. K. The difficulty for subducted oceanic crust to accumulate at the Earth's core–mantle boundary. *J. Geophys. Res.* **118**, 1807–1816 (2013).
- Hallis, L. J. *et al.* Evidence for primordial water in Earth's deep mantle. *Science* **350**, 795–797 (2015).
- Walter, M. J. *et al.* The stability of hydrous silicates in Earth's lower mantle: experimental constraints from the systems $\text{MgO-SiO}_2\text{-H}_2\text{O}$ and $\text{MgO-Al}_2\text{O}_3\text{-SiO}_2\text{-H}_2\text{O}$. *Chem. Geol.* **418**, 16–29 (2015).
- Peacock, S. A. Fluid processes in subduction zones. *Science* **248**, 329–337 (1990).
- van Keken, P. E., Hacker, B. R., Syracuse, E. M. & Abers, G. A. Subduction factory: 4. Depth-dependent flux of H_2O from subducting slabs worldwide. *J. Geophys. Res.* **116**, 2156–2202 (2011).
- Okuchi, T. Hydrogen partitioning into molten iron at high pressure: implications for Earth's core. *Science* **278**, 1781–1784 (1997).
- Lobanov, S. S. *et al.* Stable magnesium peroxide at high pressure. *Sci. Rep.* **5**, 13582 (2015).
- Sinmyo, R. *et al.* Discovery of Fe_2O_9 : a new iron oxide with a complex monoclinic structure. *Sci. Rep.* **6**, 32852 (2016).
- Iizuka-Oku, R. *et al.* Hydrogenation of iron in the early stage of Earth's evolution. *Nat. Commun.* **8**, 14096 (2017).
- Liu, J. *et al.* Iron isotopic fractionation between silicate mantle and metallic core at high pressure. *Nat. Commun.* **8**, 14377 (2017).

Acknowledgements We thank A. Shahar for providing the ^{57}Fe -enriched hematite (Fe_2O_3 with ^{57}Fe of >96.5%) powder samples. We acknowledge C. Kenney-Benson, L. X. Yang, T. T. Gu, B. Li, W. G. Yang, Y. Wu, B. Chen, E. Ohtani, X. Y. Tong and M. M. Li for experimental assistance and discussion, and E. Greenberg for beamline technical support. NRIXS and XRD measurements were performed at the High Pressure Collaborative Access Team (HPCAT 16-IDB and 16-IDD), Advanced Photon Source, Argonne National Laboratory. Some of the XRD experiments were performed at GeoSoilEnviroCARS (Sector 13ID-D) at the Advanced Photon Source. HPCAT operations are supported by the Department of Energy (DOE)-NNSA under award DE-NA0001974, with partial instrumentation funding by NSF. Y.X., P.C. and Y.M. acknowledge the support of the DOE-BES/DMSE under award DE-FG02-99ER45775. GeoSoilEnviroCARS is supported by the National Science Foundation (NSF)—Earth Sciences (EAR-1128799) and the DOE Geosciences (DE-FG02-94ER14466). Use of the Advanced Photon Source was supported by the US DOE, Office of Science, Office of Basic Energy Sciences, under contract number DE-AC02-06CH11357. W.L.M., Q.H. and J.L. acknowledge support from the Geophysics Program by the NSF (EAR 1446969) and the Deep Carbon Observatory. H.-K.M. and Q.H. were supported by NSF grants EAR-1345112 and EAR-1447438. This work was also partially supported by the National Natural Science Foundation of China (grant number U1530402). Some of the computations were conducted at the Supercomputing Center of the University of Science and Technology of China. Z.W. and W.W. acknowledge the support of the Natural Science Foundation of China (41590621) and State Key Development Program of Basic Research of China (2014CB845905). We thank M. Walter for comments and suggestions.

Author Contributions J.L., Q.H., Y.X., Y.M., V.B.P. and P.C. carried out the experiment. J.L., W.L.M. and H.-K.M. performed the experimental data analysis. D.Y.K., Q.H., Z.W. and W.W. performed the theoretical simulation. H.-K.M. and W.L.M. conceived and designed the project and directed the calculations and experiments. J.L., W.L.M. and H.-K.M. wrote the manuscript. All authors contributed to the discussion of the results and revision of the manuscript.

Author Information Reprints and permissions information is available at www.nature.com/reprints. The authors declare no competing financial interests. Readers are welcome to comment on the online version of the paper. Publisher's note: Springer Nature remains neutral with regard to jurisdictional claims in published maps and institutional affiliations. Correspondence and requests for materials should be addressed to W.L.M. (wmao@stanford.edu) and H.-K.M. (hmao@gl.ciw.edu).

Reviewer Information Nature thanks M. Walter and the other anonymous reviewer(s) for their contribution to the peer review of this work.

METHODS

Sample synthesis. The starting material hematite (Fe_2O_3) is ^{57}Fe -enriched (with ^{57}Fe of $>96.5\%$) because the NRIXS technique is sensitive to the Mössbauer isotope ^{57}Fe . The ^{57}Fe -enriched Fe_2O_3 was purchased from Cambridge Isotope Laboratories. A beryllium gasket 3 mm in diameter was pre-indented to 18–19 GPa between a pair of diamond anvils with 150–300 μm bevelled culets that were used in a DAC to reach pressures of over one megabar. Cubic boron nitride was placed as an inner gasket insert to keep the sample as thick as possible under extreme conditions. A hole of 80–90 μm in diameter was drilled in the centre as a sample chamber using a laser drill system at the HPCAT³¹. A platelet of hematite sample 25–35 μm in diameter and about 10 μm thick was loaded into the sample chamber together with a small piece of gold (Au) about 10 μm in diameter and/or a ruby sphere as the pressure maker. For synthesizing pure iron peroxide, the DAC was placed in a sealed copper container that was immersed in liquid nitrogen. The container was fluxed with oxygen gas that would be liquefied. Once the level of liquid oxygen reached above the diamond anvil table on the cylinder side, liquid oxygen would be entrapped in the sample chamber after the DAC was sealed. FeO_2 was then synthesized by laser heating at approximately 80 GPa. XRD patterns were collected and confirmed to form FeO_2 in the pyrite structure. The Fe_2O_3 starting sample fully reacted with oxygen to form FeO_2 after laser heating at 1,800–2,000 K for approximately 1.5 h. On the other hand, for synthesizing FeO_2H_x , we loaded high-quality pure deionized water into the sample chamber, instead of liquid oxygen, to react with Fe_2O_3 to form FeO_2H_x at high pressure and high temperature. The sample was fully transformed into FeO_2H_x in the pyrite-type structure at relatively higher pressures of 90–100 GPa and higher temperatures of 2,000–2,200 K with laser heating for around 2 h.

Synchrotron XRD experiments. XRD measurements were conducted at beamlines 16-IDB and 13-IDD of the Advanced Phonon Source, Argonne National Laboratory. A highly monochromatized incident X-ray beam was used with an energy of 33.17 keV (0.3738 Å) for the former and 37.08 keV (0.3344 Å) for the latter. The incident X-ray beam was focused down to a beam size of 2–5 μm in the full-width at half-maximum (FWHM) at sample position. For laser-heating XRD experiments, two infrared laser beams were focused down to 20–30 μm in FWHM on both sides of the sample and they were co-axially aligned with the incident X-ray beam using the X-ray induced luminescence on the sample and/or ruby^{32,33}. The temperature of the heated samples was calculated through fitting the measured thermal radiation spectra with the grey-body approximation and its uncertainty was ± 100 –200 K on the basis of multiple temperature measurements on both sides. Pressure and its uncertainty were determined from the lattice parameters of Au³⁴. **NRIXS experiments.** High-pressure NRIXS experiments on FeO_2 and FeO_2H_x in DACs at 81–133 GPa were performed at the beamline 16-IDD, Advanced Photon Source, Argonne National Laboratory. A symmetric DAC was modified and had four enlarged side openings that allowed access to the four avalanche photodiode detectors. Each NRIXS spectrum was scanned around the nuclear transition energy of 14.4125 keV of the ^{57}Fe isotope with a step size of 0.5 meV or 0.6 meV and a collection time of 10 s per energy step. The X-ray beam bandwidth is 2 meV. Each NRIXS scan took approximately 1.5 h. Owing to the extremely low NRIXS single count rate for FeO_2 at 81 GPa and FeO_2H_x at 133 GPa and 300 K, about 65 NRIXS scans per pressure point (approximately 3–4 days of beamtime) were collected and co-added together to achieve good statistics (Extended Data Table 1). The measured NRIXS spectra were processed using the PHOENIX software (version 2.1.3)³⁵. It removed the elastic contribution and applied the quasi-harmonic lattice model to extract the partial PDOS of the ^{57}Fe isotope in the aggregate samples (inset to Fig. 3)³⁵. The low-energy portion of the PDOS can be used to derive the Debye sound velocity (V_D) using the Debye model. The low-energy range of the PDOS was determined using the best fit in the χ^2 analysis and then used to derive V_D (Fig. 3). Using the V_D from NRIXS measurements and the density (ρ) and isothermal bulk modulus (K_T) data from the equation of state of the sample, the aggregate V_P and V_S of the sample can be calculated from the following equations:

$$\frac{3}{V_D^3} = \frac{1}{V_P^3} + \frac{2}{V_S^3} \quad (1)$$

$$K_S = \rho \left(V_P^2 - \frac{4}{3} V_S^2 \right) \quad (2)$$

and

$$G = \rho V_S^2 \quad (3)$$

where the adiabatic bulk modulus K_S is approximated by K_T , which is usually smaller than K_S by about 1%. The Raman spectra of the diamond anvils were used as a pressure gauge³⁶, while the highest pressure of 133 GPa for FeO_2H_x was

cross-checked with the equation of state³⁴ of Au. The Poisson ratio (ν) is then determined from:

$$\nu = \frac{V_P^2 - 2V_S^2}{2(V_P^2 - V_S^2)} \quad (4)$$

Theoretical simulations. Isothermal elastic tensors of materials can be calculated from³⁷:

$$C_{ijkl}^T = \frac{1}{V} \left(\frac{\partial^2 F}{\partial e_{ij} \partial e_{kl}} \right) + \frac{1}{2} P (2\delta_{ij}\delta_{kl} - \delta_{il}\delta_{kj} - \delta_{ik}\delta_{jl}) \quad (5)$$

Here, e_{ij} ($i, j = 1, 3$) are infinitesimal strains and F is the Helmholtz free energy, which is expressed in the quasi-harmonic approximation as:

$$F(e_{ij}, V, T) = U(e_{ij}, V) + \frac{1}{2} \sum_{q,m} \hbar \omega_{q,m}(e_{ij}, V) + k_B T \sum_{q,m} \ln \left[1 - \exp \left(- \frac{\hbar \omega_{q,m}(e_{ij}, V)}{k_B T} \right) \right] \quad (6)$$

where q is the phonon wave vector, m is the normal index, $\omega_{q,m}$ is the vibrational frequency of the system, and \hbar and k_B are the Planck and Boltzmann constants, respectively. The first, second and third terms in equation (6) are the static internal, zero-point and vibrational energy contributions under temperature T at equilibrium volume V , respectively. Calculations of elastic moduli using this frequently used method require the vibrational frequencies of many strained configurations, thus making calculations of elasticity at high temperatures and pressures costly. A semianalytical approach to calculating the thermal contribution to elastic tensors has been proposed³⁸ that requires only the vibrational density of states for unstrained configurations and static elasticity. This approach reduces the computation time to the level of no more than 10% of the usual method without loss of accuracy.

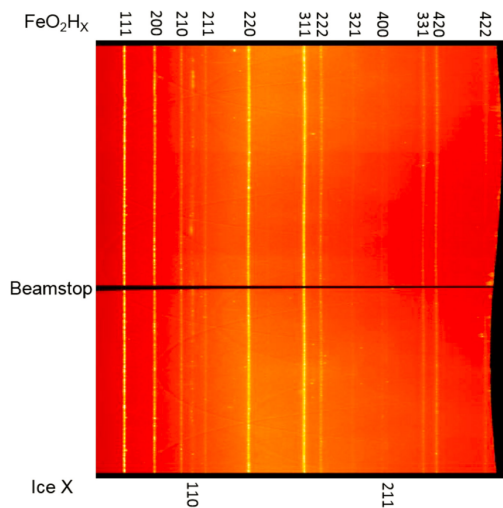
To obtain the vibrational density of states for unstrained configurations and static elasticity at different volumes, we performed first-principles calculations using the Quantum Espresso package³⁹ based on density functional theory, adopting a generalized gradient approximation (GGA) for the exchange correlation function. Electronic wavefunctions were expanded by a plane-wave basis with an energy cutoff of 80 Ry and a charge density of 800 Ry. The pseudopotentials for iron and hydrogen, Fe.pbe-spn-kjpaw_psl.0.2.1.UPF and H.pbe-kjpaw_psl.0.1.UPF, which are available in the online Quantum Espresso pseudopotential library (<http://www.quantum-espresso.org/pseudopotentials/>), were generated using the Projector augmented-wave method^{40,41}. A norm-conserving pseudopotential was used for oxygen generated by the Troullier–Martins method⁴² with a valence configuration of $2s^2 2p^4$. Owing to the insufficient treatment of the large on-site Coulomb interactions among the localized electrons (Fe $3d$ electrons)⁴³, to obtain more reliable results, we followed the strategy previous studies^{43–46} have taken that introduces a Hubbard U correction to the GGA for the all calculations of FeO_2 and FeO_2H . U values were non-empirically determined using the linear response method⁴⁷. The crystal structure for a particular volume was well optimized on a $12 \times 12 \times 12$ k -point mesh and then the phonon frequencies were calculated using the *ab initio* lattice dynamics⁴⁸ method, which is based on GGA + U . The static elastic constants could be calculated from the second derivatives of the free energy as a function of small strains⁴⁹.

To calculate the PDOS and the equations of state, we conducted first-principles calculations using the VASP package⁵⁰ based on density functional theory and Phonopy⁵¹ for Quasi-Harmonic Approximation (QHA). We use the generalized approximation by Perdew, Burke and Ernzerhof (the PBE GGA) for the exchange correlation^{52,53} with a plane-wave cutoff of 875 eV and a $12 \times 12 \times 12$ k -point mesh. To treat the $3d$ electrons of Fe properly, we also used the DFT + U approach⁵⁴ and we used the on-site Coulomb interaction and Hund coupling constant⁵⁵. The Helmholtz free energies calculated from the static energy and vibrational density of state (equation (6)) using the QHA versus volume were fitted by isothermal third-order finite strain equations of state. Thus, we can calculate all thermodynamic properties, including pressures at different temperatures and volumes derived from the Helmholtz free energies, and transfer volume- and temperature-dependent elasticity into pressure- and temperature-dependent elasticity based on the equation of state.

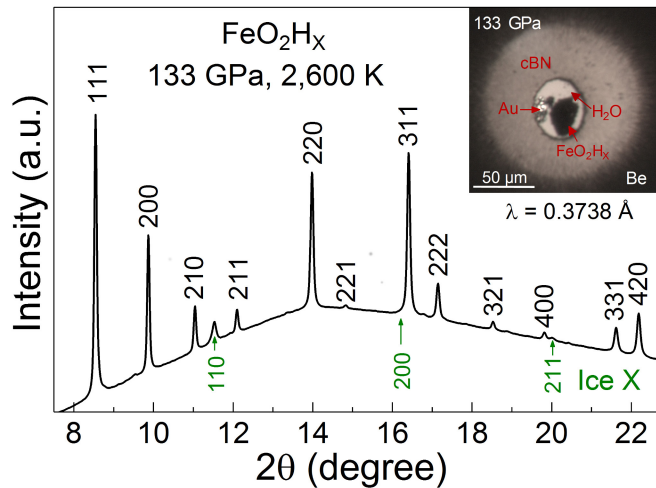
Data availability. The data that support the findings of this study are available from the corresponding authors on reasonable request.

30. Narygina, O. *et al.* X-ray diffraction and Mössbauer spectroscopy study of fcc iron hydride FeH at high pressures and implications for the composition of the Earth's core. *Earth Planet. Sci. Lett.* **307**, 409–414 (2011).

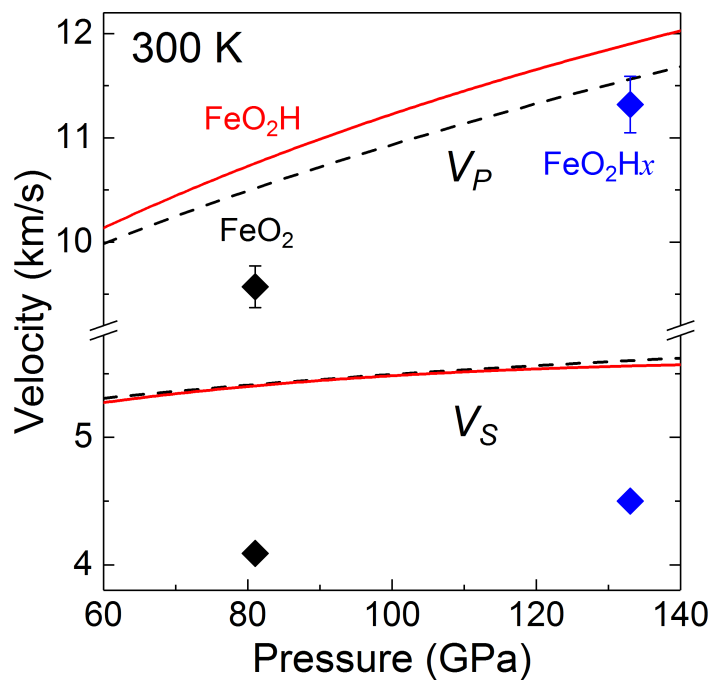
31. Hrubiak, R., Sinogeikin, S., Rod, E. & Shen, G. The laser micro-machining system for diamond anvil cell experiments and general precision machining applications at the High Pressure Collaborative Access Team. *Rev. Sci. Instrum.* **86**, 072202 (2015).
32. Prakapenka, V. B. *et al.* Advanced flat top laser heating system for high pressure research at GSECARS: application to the melting behavior of germanium. *High Press. Res.* **28**, 225–235 (2008).
33. Meng, Y., Hrubiak, R., Rod, E., Boehler, R. & Shen, G. New developments in laser-heated diamond anvil cell with *in situ* synchrotron x-ray diffraction at High Pressure Collaborative Access Team. *Rev. Sci. Instrum.* **86**, 072201 (2015).
34. Fei, Y. *et al.* Toward an internally consistent pressure scale. *Proc. Natl Acad. Sci. USA* **104**, 9182–9186 (2007).
35. Sturhahn, W. CONUSS and PHOENIX: evaluation of nuclear resonant scattering data. *Hyperfine Interact.* **125**, 149–172 (2000).
36. Akahama, Y. & Kawamura, H. Pressure calibration of diamond anvil Raman gauge to 410 GPa. *J. Phys. Conf. Ser.* **215**, 012195 (2010).
37. Barron, T. H. K. & Klein, M. L. Second-order elastic constants of a solid under stress. *Proc. Phys. Soc.* **85**, 523–532 (1965).
38. Wu, Z. & Wentzcovitch, R. M. Quasiharmonic thermal elasticity of crystals: an analytical approach. *Phys. Rev. B* **83**, 184115 (2011).
39. Giannozzi, P. *et al.* QUANTUM ESPRESSO: a modular and open-source software project for quantum simulations of materials. *J. Phys. Condens. Matter* **21**, 395502 (2009).
40. Blöchl, P. E. Projector augmented-wave method. *Phys. Rev. B* **50**, 17953–17979 (1994).
41. Kresse, G. & Joubert, D. From ultrasoft pseudopotentials to the projector augmented-wave method. *Phys. Rev. B* **59**, (1999).
42. Troullier, N. & Martins, J. L. Efficient pseudopotentials for plane-wave calculations. II. Operators for fast iterative diagonalization. *Phys. Rev. B* **43**, 8861–8869 (1991).
43. Anisimov, V. I., Zaanen, J. & Andersen, O. K. Band theory and Mott insulators: Hubbard U instead of Stoner I. *Phys. Rev. B* **44**, 943–954 (1991).
44. Fukui, H., Tsuchiya, T. & Baron, A. Q. R. Lattice dynamics calculations for ferropericase with internally consistent LDA+U method. *J. Geophys. Res.* **117**, B12202 (2012).
45. Metsue, A. & Tsuchiya, T. Thermodynamic properties of (Mg,Fe²⁺)SiO₃ perovskite at the lower-mantle pressures and temperatures: an internally consistent LSDA+U study. *Geophys. J. Int.* **190**, 310–322 (2012).
46. Tsuchiya, T. & Wang, X. Ab initio investigation on the high-temperature thermodynamic properties of Fe³⁺-bearing MgSiO₃ perovskite. *J. Geophys. Res.* **118**, 83–91 (2013).
47. Cococcioni, M. & de Gironcoli, S. Linear response approach to the calculation of the effective interaction parameters in the LDA+U method. *Phys. Rev. B* **71**, 035105 (2005).
48. Alfè, D. PHON: A program to calculate phonons using the small displacement method. *Comput. Phys. Commun.* **180**, 2622–2633 (2009).
49. Mehl, M. J., Osburn, J. E., Papaconstantopoulos, D. A. & Klein, B. M. Structural properties of ordered high-melting-temperature intermetallic alloys from first-principles total-energy calculations. *Phys. Rev. B* **41**, 10311–10323 (1990).
50. Kresse, G. & Furthmüller, J. Efficient iterative schemes for ab initio total-energy calculations using a plane-wave basis set. *Phys. Rev. B* **54**, 11169–11186 (1996).
51. Togo, A. & Tanaka, I. First principle phonon calculations in materials science. *Scr. Mater.* **108**, 1–5 (2015).
52. Perdew, J. P. *et al.* Atoms, molecules, solids, and surfaces: applications of the generalized gradient approximation for exchange and correlation. *Phys. Rev. B* **46**, 6671–6687 (1992).
53. Perdew, J. P., Burke, K. & Ernzerhof, M. Generalized gradient approximation made simple. *Phys. Rev. Lett.* **77**, 3865–3868 (1996).
54. Dudarev, S. L., Botton, G. A., Savrasov, S. Y., Humphreys, C. J. & Sutton, A. P. Electron-energy-loss spectra and the structural stability of nickel oxide: an LSDA+U study. *Phys. Rev. B* **57**, 1505–1509 (1998).
55. Jang, B. G., Kim, D. Y. & Shim, J. H. Metal-insulator transition and the role of electron correlation in FeO₂. *Phys. Rev. B* **95**, 075144 (2017).



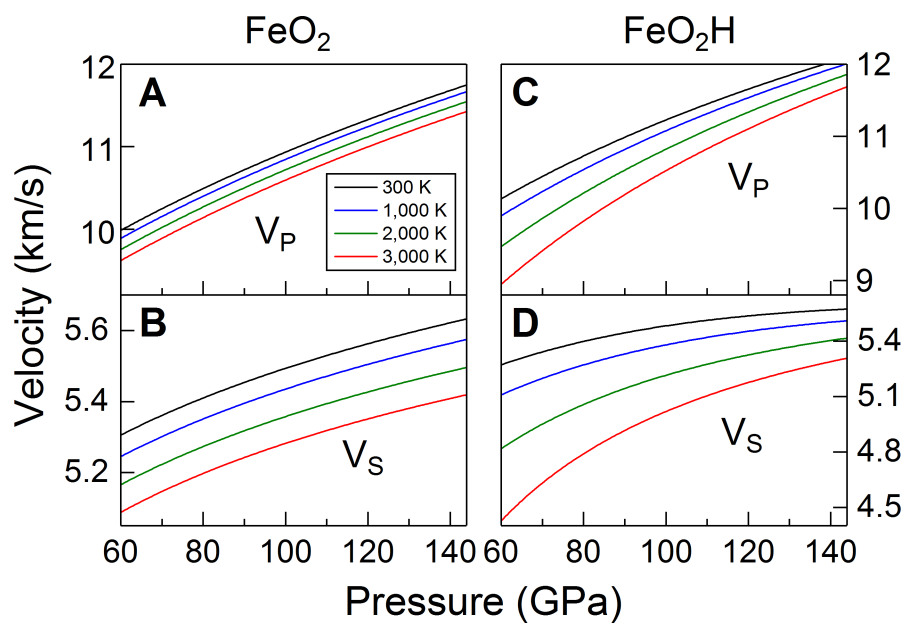
Extended Data Figure 1 | XRD pattern of FeO_2H_x at 133 GPa and 2,600 K. The sharp diffraction lines in the integrated pattern (right panel) are from the synthesized FeO_2H_x and H_2O (ice X). FeO_2H_x was first synthesized from Fe_2O_3 and H_2O at 90–100 GPa and 2,000–2,200 K. XRD patterns were collected with increasing pressure up to 133 GPa. At each increasing pressure step, the sample was laser annealed to 2,000 K to release any possible deviatoric strain that may have developed. Miller indices (hkl) for FeO_2H_x in the pyrite structure are labelled above



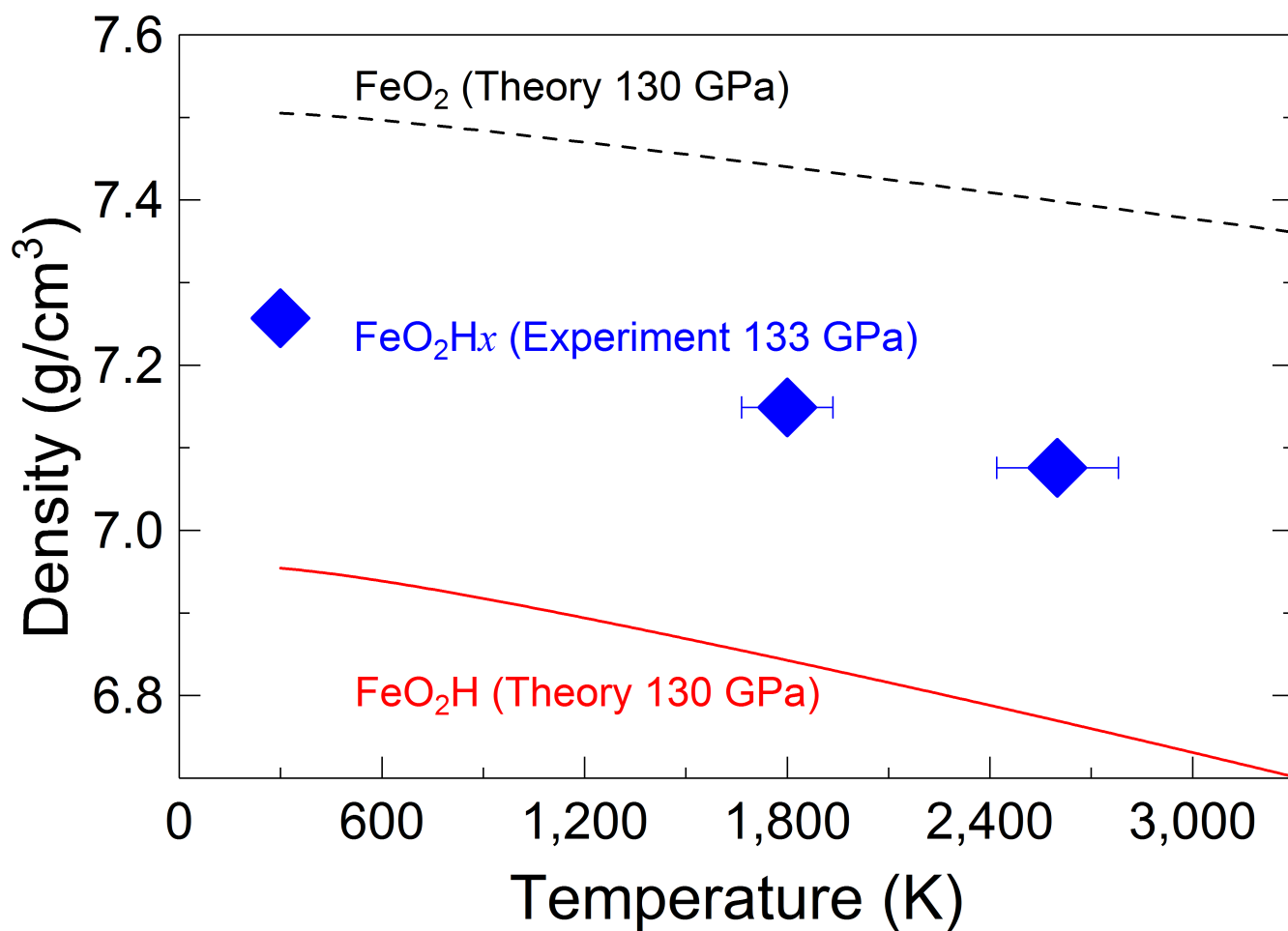
corresponding peaks. Green arrows indicate locations of peaks for H_2O in the ice X structure. The inset shows a photomicrograph of the sample chamber at 133 GPa after laser heating at 2,600 K. The sample was surrounded by a cubic boron nitride (cBN) gasket insert. A two-dimensional XRD image (left panel) of FeO_2H_x was collected at 133 GPa and 300 K after laser heating, which corresponds to the integrated XRD pattern. Source Data for Extended Data Figs 1–4 accompany the online version of the paper.



Extended Data Figure 2 | Sound velocities of FeO_2H_x at high pressure and 300 K. Filled symbols show the V_P and V_S of FeO_2 at 81 GPa (black) and FeO_2H_x at 133 GPa (blue) from NRIXS experiments; solid and dashed curves show FeO_2 (black) and FeO_2H (red) as a function of pressure from theoretical calculations. All error bars are derived from standard error propagation and represent $\pm 1\sigma$. Error bars smaller than the symbols are not shown for clarity.



Extended Data Figure 3 | Temperature effects on V_P and V_S of FeO_2 and FeO_2H . Sound velocities of FeO_2 (a, b) and FeO_2H (c, d) at high pressure and high temperature obtained by theoretical calculations.



Extended Data Figure 4 | Density of FeO₂H_x as a function of temperature at CMB pressures. Diamonds show FeO₂H_x at 133 GPa from XRD experiments; black and red curves show FeO₂ and FeO₂H at 130 GPa,

respectively, from theoretical calculations. All error bars are derived from standard error propagation and represent $\pm 1\sigma$. Error bars of the density derived from XRD experiments are smaller than the symbol.

Extended Data Table 1 | Sound velocities of FeO₂ and FeO₂H_x at high pressure

Pressure (GPa)	Energy Range (meV) [†]	V_P (km/s)	V_S (km/s)	Poisson's Ratio
FeO ₂				
81 (±2)	-75 to +85	9.57 (±0.20)	4.09 (±0.06)	0.39
FeO ₂ H _x				
133 (±4)	-85 to +95	11.32 (±0.27)	4.50 (±0.07)	0.41

High-pressure NRIXS measurements were conducted at room temperature.

[†]The energy range over which NRIXS data was collected is relative to the nuclear transition energy of ⁵⁷Fe (14.4125 keV). The energy resolution is 2 meV. The scan step size was 0.5 meV.